



## Revisiting thermodynamics and kinetic diffusivities of uranium–niobium with Bayesian uncertainty analysis



Thien C. Duong<sup>a,\*</sup>, Robert E. Hackenberg<sup>c</sup>, Alex Landa<sup>d</sup>, Pejman Honarmandi<sup>a</sup>, Anjana Talapatra<sup>a</sup>, Heather M. Volz<sup>c</sup>, Anna Llobet<sup>c</sup>, Alice I. Smith<sup>c</sup>, Graham King<sup>c</sup>, Saurabh Bajaj<sup>b</sup>, Andrei Ruban<sup>e</sup>, Levente Vitos<sup>e</sup>, Patrice E.A. Turchi<sup>d</sup>, Raymundo Arróyave<sup>a</sup>

<sup>a</sup> Materials Science and Engineering, Texas A & M University, College Station, TX 77843, USA

<sup>b</sup> Environmental Energy & Technologies Division, Lawrence Berkeley National Laboratory, Berkeley, CA 94720, USA

<sup>c</sup> Los Alamos National Laboratory, P.O. Box 1663, Los Alamos, NM 87545, USA

<sup>d</sup> Lawrence Livermore National Laboratory, Livermore, CA 94550, USA

<sup>e</sup> Royal Institute of Technology, Valhallavägen 79, Stockholm, Sweden

### ARTICLE INFO

#### Article history:

Received 11 May 2016

Received in revised form

15 September 2016

Accepted 16 September 2016

Available online 20 September 2016

#### Keywords:

DFT

CALPHAD

Bayesian

Uncertainty analysis

Metallic fuels

U–Nb

Thermodynamics

Kinetic diffusivity

### ABSTRACT

In this work, thermodynamic and kinetic diffusivities of uranium–niobium (U–Nb) are re-assessed by means of the CALPHAD (CALculation of PHase Diagram) methodology. In order to improve the consistency and reliability of the assessments, first-principles calculations are coupled with CALPHAD. In particular, heats of formation of  $\gamma$ -U–Nb are estimated and verified using various density-functional theory (DFT) approaches. These thermochemistry data are then used as constraints to guide the thermodynamic optimization process in such a way that the mutual-consistency between first-principles calculations and CALPHAD assessment is satisfactory. In addition, long-term aging experiments are conducted in order to generate new phase equilibria data at the  $\gamma_2/\alpha + \gamma_2$  boundary. These data are meant to verify the thermodynamic model. Assessment results are generally in good agreement with experiments and previous calculations, without showing the artifacts that were observed in previous modeling. The mutual-consistent thermodynamic description is then used to evaluate atomic mobility and diffusivity of  $\gamma$ -U–Nb. Finally, Bayesian analysis is conducted to evaluate the uncertainty of the thermodynamic model and its impact on the system's phase stability.

Published by Elsevier Ltd.

### 1. Introduction

Over the years, U–Nb has been known to be a promising nuclear fuel for Gen-IV fast breeder reactors. The material exhibits a high melting point, good corrosion resistance, good conductivity and a continuous bcc region at high temperatures. This, in principle, would introduce thermal and mechanical stability during the thermal operation of the reactor, given that the desired fuel exists in the form of pure-bcc single- or polycrystals. In reality, depending on its heat treatment conditions, various forms of metastable phases exist as different microstructures within the bcc matrix, among which some lead to the fuel's enhancements while others to its degradation. For example, during the monotectoid decomposition of U–Nb, a quenched  $\gamma_1$  (U-rich bcc) does not decompose continuously into the end equilibria of  $\alpha$  (orth) and  $\gamma_2$  (U-depleted bcc). Instead, it tends to transform into different

intermediate states depending on its heat treatment condition. Aging at  $\sim 300^\circ\text{C}$  and lower results in significant age-hardening accompanied by subtle microstructural changes (e.g., [1–4]). Under these conditions, the system remains distant from thermodynamic equilibrium even after long-term ( $\sim 5$  years) aging and the specific transformation mechanisms remain unresolved. The microstructural evolution upon aging at higher temperatures ( $300$ – $647^\circ\text{C}$ ) has been more definitively characterized. In particular, the system accesses a mixture of  $\alpha$  phase plus a metastable phase of an intermediate Nb composition with the same bcc crystal structure as the stable  $\gamma_2$  phase [5]. This mixture has a lamellar structure and is associated with the so-called cellular reaction [6]. After further prolonged annealing, the metastable  $\gamma_{1-2}$  transforms into the final mixture of  $\alpha$  and  $\gamma_2$  when stable  $\gamma_2$  nucleates inside the system, and the lamellar structure coarsens. Under these structural changes, the material is known to undergo considerable degradations in terms of strength, ductility, and corrosion resistance [2].

Understanding the origins and mechanisms of these microstructure evolutions is key to the evaluation and, in an ambitious

\* Corresponding author.

E-mail address: [terryduong84@tamu.edu](mailto:terryduong84@tamu.edu) (T.C. Duong).

and optimistic vision, engineering of the fuel's macroscopic properties and performance. Given that U–Nb is a promising fuel candidate, such an understanding is found to be relevant to the national interest in the research and development of nuclear energy as a promising clean and sustainable energy resource for social development. In order to build up such an understanding of the microstructure evolutions, the essential first step is to establish a sound background of fundamental thermodynamics and kinetic diffusivities of the material. This background, in the long run, can also serve as prerequisite to understanding the Nb-based fuel—cladding interactions, or assessing the properties and performance of advanced multi-component metallic fuels, built upon the binary fuel (e.g. U–Zr–Nb), hence benefiting further the national interest. The present work, as such, seeks to contribute to the establishment of the background of fundamental thermodynamics and kinetic diffusivities of U–Nb by means of first-principles calculations, CALPHAD assessments, XRD experiments, and Bayesian uncertainty analysis.

Before moving on to details, it is noted that the CALPHAD thermodynamic assessment of U–Nb has already been conducted by Liu et al. [7], and its result was later used by Liu et al. [8] to estimate the atomic mobilities of  $\gamma$  also within the CALPHAD framework. Even though the thermodynamic study [7], on which the kinetic work [8] is based, shows good phase equilibria under the liquidus line, consistent with previous evaluations and experiments [9–12], extrapolation of  $\gamma$ -free energy to temperatures above 5000 °C results in an inverse miscibility gap, manifested in the metastable diagram of the bcc phase. As indicated by Bajaj et al. [13], although this phenomenon is thermodynamically possible and such features are found in various polymer systems, it is likely an assessment artifact in simple metallic alloys. They have pointed out that CALPHAD's parameter optimization is an inverse problem that has many possible solutions among which some may contain unreasonable "hidden" phase stabilities. The use of ab initio energetic data can impose a restriction on the CALPHAD optimization and hence reduce the probability of encountering artifacts. This is in accordance with the spirit of the Ringberg workshops on the relations between first-principles calculations and CALPHAD modeling during the years from 1996 to 1999 [14–16].

In the present work, we practice the mutual-consistent assessment strategy, coupling first-principles calculations with CALPHAD methodology, as suggested in [13]. In particular, first-principles calculations are conducted within the framework of Density Functional Theory (DFT) to estimate for the ground-state heats of formation of  $\gamma$ . The ab initio energies are then combined with experimental equilibria to re-assess the fundamental thermodynamics of U–Nb via CALPHAD. Assessment results are overall in reasonable agreement with the work of Liu et al. [7] without producing the inverse miscibility gap. Their reliability is further checked against our supplementary equilibria of the  $\gamma_2/\alpha + \gamma_2$  phase boundary measured by sufficient long-term aging experiments (up to 5 years). The achieved thermodynamic data is then used to re-evaluate the kinetic diffusivities of  $\gamma$  described in terms of atomic mobilities [17] also within the framework of CALPHAD. Finally, model uncertainty is analyzed via Bayesian Monte-Carlo simulation. The detailed discussions are presented in the following.

## 2. First-principles calculations of $\gamma$ 's formation energies

### 2.1. Computational details

For the first-principles investigations in the present work, we utilize two different Green's function approaches, namely

Korringa–Kohn–Rostoker (KKR) multiple scattering formalism and exact muffin-tin orbital (EMTO) method. The self-consistent calculations are performed within the scalar-relativistic regime for a basis set of *spdf* valence orbitals. The core states are recalculated at every ionic step according to the soft-core approximation. Generalized gradient approximation (GGA) is adopted for the exchange-correlation functional [59]. The integration over the Brillouin zone is done using a  $31 \times 31 \times 31$  grid of k-points determined according to the Monkhorst–Pack scheme [18]. Integration of the Green function is carried out over a complex energy contour with a 2.6Ry diameter using a Gaussian integration technique with 40 points on a semi-circle enclosing the occupied states. The substitutional disorder of the alloys is treated by using the coherent potential approximation (CPA) [19]. The applicability of CPA is checked in supercell calculations realized by the locally self-consistent Green function (LSGF) method within the EMTO formalism [20,21]. The screening constants  $\alpha$  and  $\beta$  are found to be 0.725 and 1.088, respectively.

In addition to Green's function approaches, we also use a different DFT approach for the self-consistent energetic calculations to strengthen our first-principles investigation. Namely, the full potential projector augmented wave (PAW) method [22,23] as implemented in the Vienna ab initio simulation package (VASP) [24–26] is considered. Here, the disordered structures of U – 12.5 at.% Nb, U – 25 at. % Nb, U – 50 at. % Nb, U – 72.5 at. % Nb and U – 87.5 at. % Nb are modeled by the special quasirandom structure (SQS) technique [27] generated by Monte-Carlo algorithm using 64-atom supercells [28]. A Monkhorst–Pack mesh of  $7 \times 7 \times 7$  points (including  $\Gamma$ ) and cut-off energy of 478 eV are considered for the integration over the Brillouin zone. It is believed that the used cell size, number of k-points and cut-off energy are reasonably chosen for good accuracy of self-consistent energetic calculations. Indeed, a verification calculation, carried out for the case of U–50 at. % Nb using a 128-atom SQS supercell with a  $9 \times 9 \times 9$  grid of k-points and a cut-off energy of 550 eV, demonstrates a small energetic difference (in the order of  $\frac{1}{10}$  meV/atom) w.r.t to the previous calculation. For better results, the value of  $10^{-7}$  eV is chosen for the convergence criterion. The GGA is again used to approximate for the exchange-correlation interactions.

### 2.2. Results and discussions

To verify our first-principles approaches, concentration-dependent lattice parameters of  $\gamma$  were calculated and compared with experimental data [9]. Results, shown in Fig. 1, indicate that the proposed Green's function techniques reasonably reproduce the structural characteristics of the materials (with maximum error less than 3% after taking into account the correction from thermal expansion using the linear coefficients of thermal expansion of  $20 \times 10^{-6} K^{-1}$  and  $7.88 \times 10^{-6} K^{-1}$  around 1000 °C for pure  $\gamma$  uranium and niobium, respectively [29]). Note that for these results we did not treat the uranium's 5f-electrons as strongly correlated electrons. It has been shown in the recent work of Söderlind et al. [30] that uranium when alloyed with metals possesses weakly correlated electrons which can be adequately described within the context of DFT–GGA.

In order to reduce the computational expense, PAW were only considered for the static calculations of ground-state formation energies with lattice constants interpolated from the EMTO's verified results. Within the framework of PAW and the Green's function approaches, isostructural formation energies are evaluated according to the following formula:

$$\Delta H^\phi = {}^0E_{U_{1-x}Nb_x}^\phi - (1-x){}^0E_U^\phi - x{}^0E_{Nb}^\phi \quad (1)$$

where,  ${}^0E^\phi$  are the ground-state energies of phase  $\phi$  and  $x$  is

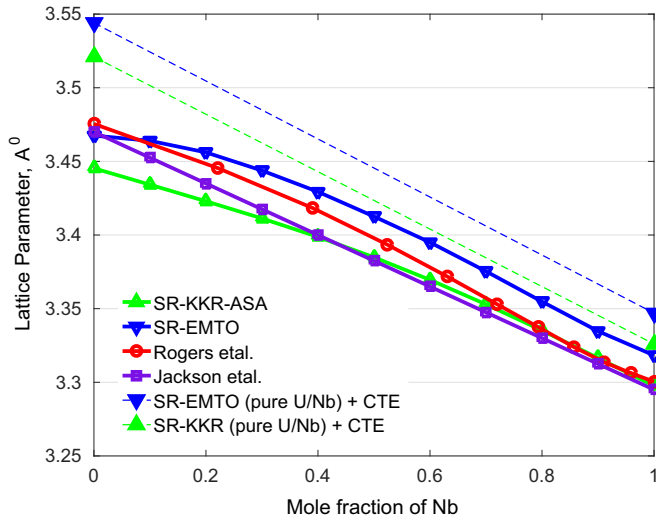


**Fig. 1.** Calculated composition-dependent lattice parameters of  $\gamma$ -bcc at 0 K as compared to experimental data from Rogers et al. [9] and Jackson et al. [31]. Note that Rogers et al. measured lattice parameters of U–Nb alloys after they were quenched from 1100 °C [9].

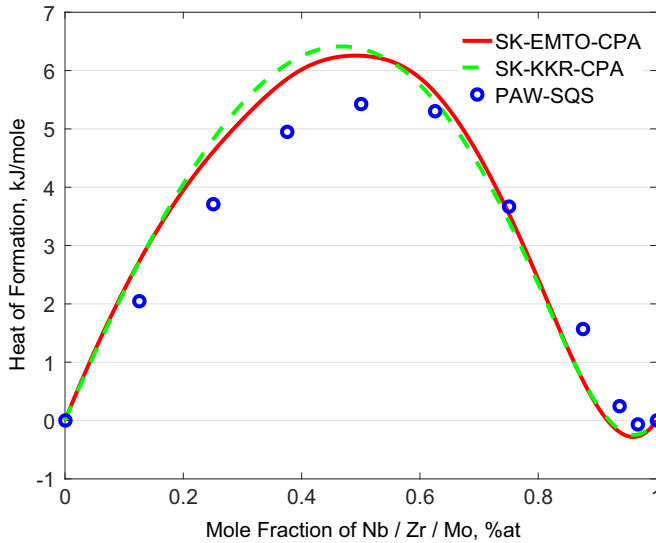


**Fig. 2.** Calculated ground-state heats of formation of  $\gamma$ -bcc using SR-EMTO, SR-KKR-ASA and PAW-SQS.

atomic fraction of Nb.

The calculated formation energies of  $\gamma$  are shown in Fig. 2. It can be seen from the figure that the first-principles results are generally in good agreement with each other. Discrepancy between PAW and Green's function methods, which is of an acceptable order of  $\sim 1.0$  kJ/mol, is perhaps due to the differences between CPA and SQS approximations. Since the energies calculated using the EMTO approach are comparable to those of KKR and tends to agree better with the system's phase diagram [11] than those of PAW calculations in terms of the exothermic behavior near the Nb-rich region, they will be selected as ab initio energetic data for the next CALPHAD assessment of the thermodynamic properties of U–Nb.

Before moving on, it is noted that for other solid states in the U–Nb system, low symmetrical structures appear to be obstacles in the density-functional estimations of their formation energies, i.e., computational costs for self-consistent energetic calculations of those structures are impractically expensive. This is especially true for the cases of Green's function approaches since both self-

consistent loops for CPA and total energy get involved. Consequently, ground-state heats of formation were not evaluated for those phases. Nevertheless, the bcc's 0 K formation energy is alone sufficient enough for imposing a solid quantum-originated constraint to the CALPHAD's optimization process, as evidenced in the following thermodynamic assessment.

### 3. CALPHAD modeling of uranium–niobium's thermodynamics

#### 3.1. Computational details

Studies of Nb-based metallic fuel mainly focus on its thermodynamic properties and many important works can be dated back to 1950s and 1960s. In particular, Sawyer [32] pioneered the studies of U–Nb phase stabilities in 1947 by sketching a nearly complete phase diagram of the material. In 1952, Saller et al. [33] focused their study on a portion of U–Nb phase diagram and proposed a change regarding the solubility of Nb in U matrix. In particular, they recommended a eutectoid instead of peritectoid reaction for the  $\beta$  –  $\gamma$  transformation. This idea was soon paced by Rogers et al. [9] whose work in 1958 is among the most comprehensive. Interestingly, in the same year (or close) another important study by Pfeil et al. [10] showed agreement with Sawyer's work. The result was obtained by applying the lever rule to the volume fraction observed from metallography in comparison to the resistivity and dilatometry measurements of Rogers et al. Discrepancies increased in 1961 when Ivanov et al. [34] proposed the monotectoid reaction occurring around 13 at.% Nb. According to them,  $\gamma$  – U should decompose into a mixture of  $\gamma$  – Nb and  $\beta$  instead of  $\gamma$  – Nb and  $\alpha$  as proposed in previous works [9,10,35]. The opinion of Ivanov et al. was later supported by Terekhov [36] and Massalski et al. [12] but disagreed by Elliott et al. [37] and Chiotti et al. [38]. In 1998, Koike et al. [11] analyzed previous works [32,39,9,10,34,40–47,36] and came up with a phase diagram evaluated by considering the most reliable experimental data. Their evaluation has been adopted in the present work in conjunction with the ab initio energetic data calculated earlier.

As a common practice, details on the parameter optimization is given in the following. Firstly, the subregular solution model [48] is considered for all U–Nb phases including  $\gamma$  (bcc),  $\alpha$  (orthorhombic),  $\beta$  (tetragonal) and liquid. Within this model, the total Gibbs free energy is expressed in terms of pure-element, ideal and excess energies, as follows:

$$G_{Nb,U:Vac}^{\phi} = \sum_{i=U,Nb} x_i {}^0G_i^{\phi} + RT \sum_{i=U,Nb} x_i \ln x_i + x_{Nb} x_U L_{Nb,U}^{\phi} \quad (2)$$

where  $\phi$  is the phase of interest,  ${}^0G_i^{\phi}$  ( $i = Nb$  or  $U$ ) is the molar Gibbs free energy of pure element obtained from the Scientific Group Thermodata Europe (SGTE) database [49], and  $x_i$  ( $i = Nb$  or  $U$ ) is the mole fraction; and  ${}^{\nu}L_{Nb,U}^{\phi}$  is the interaction parameter that accounts for the effect of non-ideality. Within the CALPHAD framework,  ${}^{\nu}L_{Nb,U}^{\phi}$  is expanded in terms of Redlich–Kister ( $r$ - $K$ ) polynomial:

$$L_{Nb,U}^{\phi} = \sum_{\nu=0}^n {}^{\nu}L_{Nb,U}^{\phi}(x_{Nb} - x_U)^{\nu} \quad (3)$$

in which,  $n$  is the number of used interaction parameters;  ${}^{\nu}L_{Nb,U}^{\phi}$  is temperature dependent and parameterized in a linear relationship as follows:

$${}^{\nu}L_{Nb,U}^{\phi} = a_{\nu}^{\phi} + b_{\nu}^{\phi}T \quad (4)$$

The  $a_{\nu}^{\phi}$  and  $b_{\nu}^{\phi}$  parameters were optimized using Thermo-Calc's

PARROT module according to the following strategy. Initially, only the bcc phase was considered. The temperature independent parts of bcc (i.e.  $a_{\gamma}^{\circ}$ ) were fitted to the EMT0 energetic data. It was found that a minimum value of 3 is required for  $n$  to reasonably reproduce the first-principles energies.  $a_{\gamma}^{\circ}$  were then kept fixed during the optimization process of  $b_{\gamma}^{\circ}$  to (1) reduce the total degrees of freedom of the PARROT's optimization process and (2) improve the consistency between CALPHAD methodology and ab initio calculations.

The optimization of temperature dependent  $b_{\gamma}^{\circ}$  was carried out by firstly introducing driving force constraints for the phase at various temperatures and concentrations, according to Koike's et al. evaluated phase diagram. This thermodynamic constraint is defined as an affinity between reacting chemical species and has a negative value where its corresponding phase is stable. The introduction of bcc's driving force constraints forged out the double-well shapes of this phase's potentials at elevated temperatures. It is noted that both Nb- and U-ends of these double-well potentials were constrained in accordance with the SGTE database [49]. At this stage, the topology of  $\gamma$ -Gibbs free energy has been properly reflected by the interaction parameters but the domain in which the energy's values can range was fairly large. To restrict this domain, Vambersky et al. [47] Gibbs formation energies, measured at 1048 K and 1173 K, were introduced.

In the following step, the  $\alpha$ ,  $\beta$  and liquid phases—or to be precise, the interaction parameters of these phases—were brought into the optimization process, in addition to the existing bcc phase. The inclusion of these additional phases further tuned up the curvature of  $\gamma$ -Gibbs free energy, as well as carved their own energetic profiles, in such a way that reasonable equilibria (or phase boundaries) were achieved between the pairs of  $\gamma - \alpha$ ,  $\gamma - \beta$  and  $\gamma$ -liquid, i.e. tie-line constraints being satisfied. Note that during this process, relative stabilities among the added phases must also be guaranteed. Finally,  $a_{\gamma}^{\circ}$  was allowed to relax together with other parameters for a better agreement between the calculated and reference phase diagram [11]. The resulting optimized values were reported in Table 1.

3.2. Results and discussions

Investigations of free energies within this miscibility gap show small deviations with respect to the previous calculations of Liu et al. [7], that tend to reasonably agree with Vambersky's et al. experiments [47] taking into account the experimental errors (see Fig. 3). Back extrapolation of Gibbs free energies of the bcc phase to 0 K is compatible with the first-principles energetic data with maximum deviation of the order of ~2.0 KJ/mol (see Fig. 4). In the monotectoid reaction, it can be seen from Table 2 that the Nb-content of reactant (13.3 at.% Nb) agrees very well with that evaluated by Koike et al. [11], it lies well within the suggested range for the  $\gamma$ -product (71.66 at.% Nb vs 68–72 at.% Nb) but is

Table 1  
Optimized thermodynamic parameters for U–Nb system.

Phase	Model	Parameters
Liquid		
Bcc	$(Nb, U)_1(Va)_3$	${}^0L_{Nb,U}^{bcc}: 28681.96 - 30.20 T$ ${}^1L_{Nb,U}^{bcc}: -25306.13 + 2.74 T$ ${}^2L_{Nb,U}^{bcc}: -37741.52 + 7.27 T$ ${}^3L_{Nb,U}^{bcc}: -13979.73 - 3.74 T$
Tet.	$(Nb, U)_1$	$G_{Nb}^{\beta U} = G_{Nb}^{bcc} + 21241.93$
Orth.	$(Nb, U)_1$	$G_{Nb}^{\alpha U} = G_{Nb}^{bcc} + 22505.03$

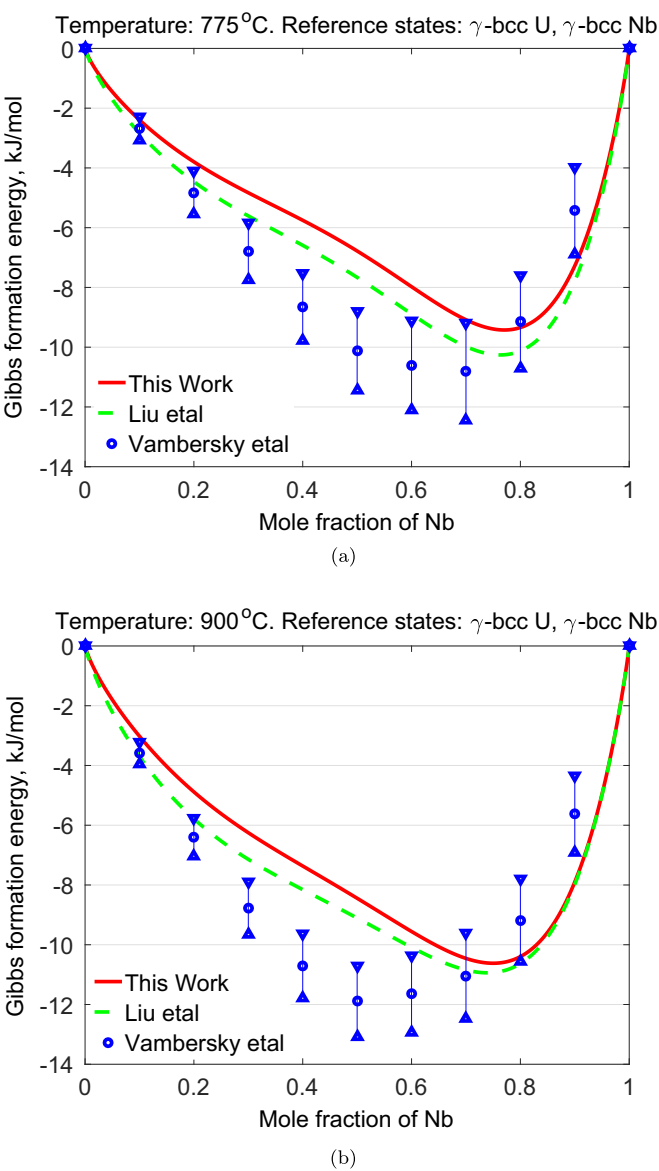


Fig. 3. CALPHAD-assessed Gibbs formation energy of bcc phase evaluated at 775 °C and 900 °C as compared to experiment [47] and previous calculation [7].

relatively high for the  $\alpha$ -product (1.3 at.% Nb vs 0.5–0.9 at.% Nb). Consequently, the  $\alpha$  phase region below this reaction is likely to overstate the solubility of Nb in U-matrix [45] although it is computationally consistent with that calculated by Liu et al. [7].

Figs. 5 and 6 show the phase diagram of U–Nb system calculated using these optimized parameters. Specifications of its invariant reactions are listed in Table 2. It can be seen from the figure that the liquidus and solidus lines agree reasonably with the experimental data [9], and as such they are compatible with those from other works [7,10,12]. Good agreement between calculations and experiments [10,43,45] is observed within the U-rich monotectoid region, in particular at the  $\beta + \gamma$  boundaries and eutectoid reaction (refer to Table 2). Near the monotectoid invariance, the  $\gamma - U + Nb$  miscibility gap appears to be slightly broader than what was evaluated by Koike et al. [11] but still within the experimental bound [9]. Also, it does not suggest a sinusoidal-like curvature as estimated in Koike et al.'s work...

Fig. 7 shows the calculated metastable phase diagram of  $\gamma$  in comparison with the one predicted by Liu et al. [7]. It can be seen from the figure that the metastable phase diagram assessed in this



Temperature: -273.15°C. Reference states:  $\gamma$ -bcc U,  $\gamma$ -bcc Nb

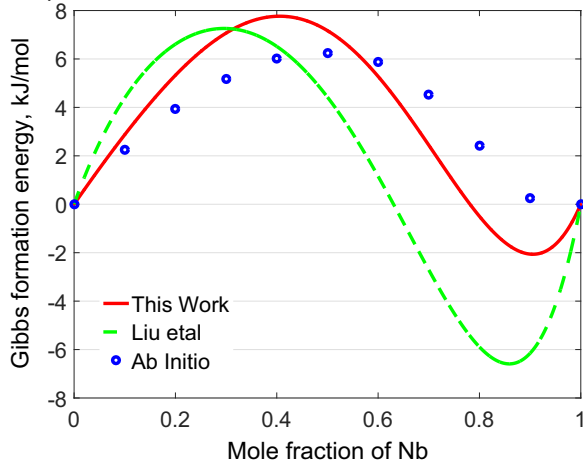


**Fig. 4.** Comparison between the current 0 K CALPHAD-assessed Gibbs formation free energy with the current first-principles energetic calculations and previous work [7]. Good agreement between CALPHAD assessment and first-principles calculation manifests a better thermodynamic consistency of the CALPHAD assessment than that of [7], which appears to be more to the experimental side (see Fig. 3).

**Table 2**

Accessed invariant reactions in comparison with previous works.

Reaction	Compositions (at.% Nb)				T (°C)	Reference
$\beta U \rightarrow \alpha U + \gamma U$	1.3	0.5 – 0.9	10.5 – 11.5	664	664	Koike et al. [11]
	1.3	1.09	10.1	664	664	Liu et al. [7]
	1.3	1.1	10.35	664	664	This work
$\gamma U \rightarrow \alpha U + (Nb)$	13.3	0.5 – 0.9	68 – 72	647	647	Koike et al. [11]
	13.9	1.3	70	647	647	Liu et al. [7]
	13.3	1.3	71.7	647	647	This work
$(\gamma U, Nb) \rightarrow \gamma U + (Nb)$	52.3			930 – 970	930 – 970	Koike et al. [11]
	50.7			958	958	Liu et al. [7]
	48.6			957	957	This work

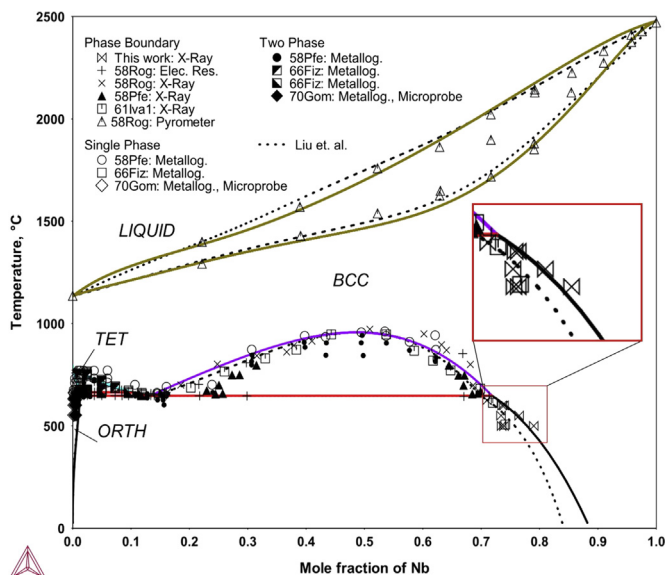


**Fig. 5.** Calculated phase diagram of U-Nb system in comparison to experimental data.

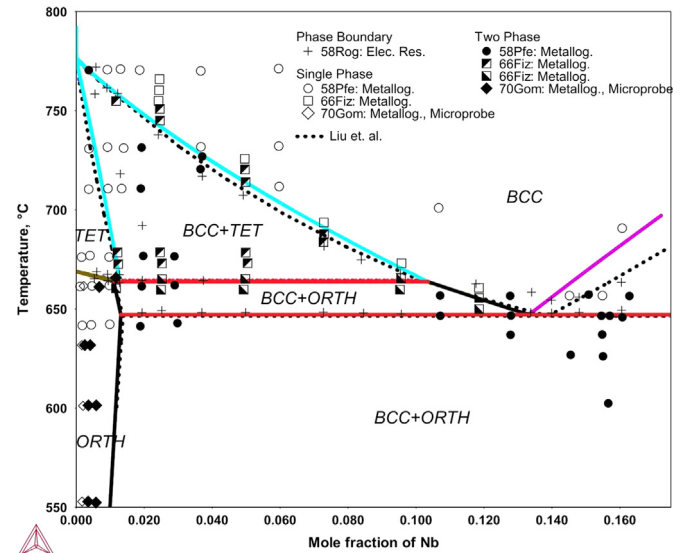


**Fig. 6.** U-rich region of the calculated phase diagram of U-Nb system.

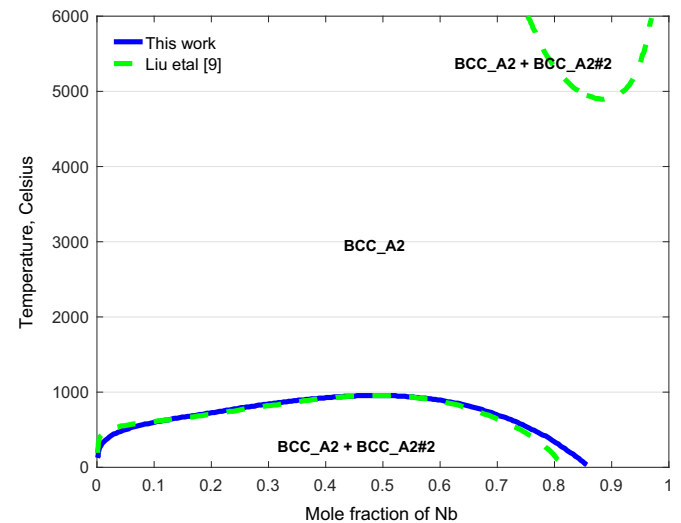


**Fig. 7.** Calculated metastable phase diagram of the bcc phase.

study does not show an inverse miscibility gap for the cubic phase as it does in Liu et al.'s work. As previously mentioned, this thermodynamic phenomenon is likely to be an assessment artifact. It has been demonstrated in [13] and the present work that the addition of first-principles energetic data to CALPHAD's optimization process has actually restrained this phenomenon and perhaps other "hidden" artifacts from existing within the solution space defined by the optimized interaction parameters.

The most important difference between the present phase diagram and its predecessor [11] lies in the specification of  $\gamma_2/\alpha + \gamma_2$  boundary. In particular, this boundary was predicted to be relatively steep in the previous work compared to its being gradual in the current study. This steep  $\gamma_2/\alpha + \gamma_2$  boundary was sketched based on the curvature of the  $\gamma - U + Nb$  miscibility boundary and two available x-ray diffraction (XRD) data-points from Ivanov et al. [34] at 500 °C and ~600 °C. Note that no explicit tempering durations were reported for these experiments; instead it was implied as being short [34]. Considering the sluggishness of U-Nb diffusion within the  $\alpha + \gamma$  region, these experimental data may not be so reliable. Indeed, Koike et al. have cautiously represented in their work a dashed-line  $\gamma_2/\alpha + \gamma_2$  boundary to indicate that further investigations are needed. In this study, X-ray diffraction (XRD)

experiments were carried out for considerably long annealing times to provide reliable  $\gamma_2/\alpha + \gamma_2$  phase-boundary data. Details of the experiments are reported in the following.

### 3.3. Experimental validation

Long-term heat treatment was conducted on specimens taken from two plates of nominal composition U-17.4 at.% Nb (chemical analysis showed 17.2 and 17.6 at.% Nb.) The alloys were vacuum induction melted from high purity depleted uranium and niobium stock, cast into graphite molds, hot rolled, and homogenized 6 h at 1000 °C. Specimens were solution annealed 30 min at 850 °C under encapsulation and water-quenched. They were re-encapsulated and then isothermally aged at over 300–625 °C for times up to 5 years. The lattice parameters (LPs) of the  $\alpha$  and  $\gamma$  phases were measured using XRD with Ceria standards and full-pattern Rietveld analysis. Specimen preparation, XRD setup, and pattern analysis were the same as that reported earlier [3].

For all aging times, the  $\alpha$ -U phase exhibited LPs close to their equilibrium value. The  $\gamma_2$  LP values varied more vs. aging, which was expected on the assumption that this variation was due to different niobium concentrations in the phase. They were converted into an equivalent Nb atom fraction  $x_{Nb}$  using the linear relationship for LP [50]:

$$LP(\gamma_2) = 3.475 - 0.175 \times x_{Nb}, \quad (5)$$

where the LP is in Angstroms. The experimental results, reported in Table 3, indicated that Nb content of  $\gamma_2$  is likely to increase with increasing aging time, and the longest experiments are actually in very good agreement with the current assessed phase boundary (refer to Fig. 5 above). In other words, they provide further evidence of the reliability of the current thermodynamic assessment. Here, it should be noted that these supplemental XRD data were only used for verification purpose, i.e., they were not included in the optimization process. This practice is known well in the field of Modeling as a method to check for the generalizations of parameterized functions, e.g., R-K polynomials within this context.

## 4. CALPHAD modeling of $\gamma$ 's atomic mobility

### 4.1. Computational details

Atomic mobilities and diffusion coefficients are of great importance in simulating and understanding the microstructure evolutions of materials. They serve, for instance, as sufficient kinetic information which together with essential thermodynamic data fulfill the prerequisites of the phase-field method [51,52]. With the achievement of the self-consistent thermodynamic description above, it naturally leaves in this section the discussion of

these kinetic quantities. Here, the  $\gamma$ 's atomic mobilities and diffusion coefficients are assessed by means of the CALPHAD methodology via the DICTRA package [53,54]. Within this approach, atomic mobility is given by [17]:

$$M_k = \frac{1}{RT} \exp\left(\frac{\Phi_k}{RT}\right), \quad (6)$$

where,  $R$  is the gas constant and  $T$  is temperature; In the CALPHAD framework,  $\Phi_k$  is expanded in term of R-K polynomial as follows:

$$\Phi_k = \sum_i x_i \Phi_k^i + \sum_i \sum_{j>i} x_i x_j \left[ \sum_r {}^r \Phi_k^{ij} (x_i - x_j)^r \right], \quad (7)$$

in which,  $\Phi_k^i$  is the mobility of the end-member;  $x$  is molar fraction; And,  ${}^r \Phi_k^{ij}$  is interaction parameter. Like in the thermodynamic assessment, these parameters are optimized in such a way that the resulting atomic mobilities can in turn yield calculated diffusivities that are comparable with experimental data. This is realized according to the relationships between diffusion coefficients and atomic mobilities among which one defines the so-called interdiffusivity [17]:

$$D_{ij}^n = \sum_{k=1}^n (\delta_{ik} - x_i) x_k M_k \left( \frac{\partial \mu_k}{\partial x_j} - \frac{\partial \mu_k}{\partial x_n} \right), \quad (8)$$

where  $\delta_{ik}$  is the Kronecker delta ( $\delta_{ik} = 1$  if  $i = k$ ; otherwise  $\delta_{ik} = 0$ ), and  $\mu_k$  is the chemical potential of element  $k$ .

The DICTRA optimization process was carried out taking into account the above self-consistent thermodynamic description. To facilitate this process, the mobility parameters of end-members were adopted from Liu et al.'s [8] work. It is noted here that the current diffusion assessment and Liu et al.'s [8] share a common goal and approach but differ fundamentally from the used thermodynamic database, i.e. in Liu et al.'s. [8] work, the PARROT optimization of Liu et al. [7] was utilized. This fundamental difference however does not tend to affect much the mobilities of end-members which are weakly dependent upon the alloy's thermodynamics. The adoption of these quantities is therefore eligible, especially when considering good agreement between calculations and experiments acquired in [8]. In contrast, the interaction parameters, which characterize chemical exchanges and correlations within the alloy system, strongly depend on the system's chemical potentials and hence are expected to alter consistently with the change of thermodynamic database. Here, the interaction parameters were optimized using the experimental tracer diffusivities taken from Adda et al. [55] and Fedorov et al. [56] and the interdiffusivities measured by Fedorov et al. [57].

**Table 4**  
Optimization kinetic parameters for the bcc phase of U–Nb system.

Model	Mobility	Parameters
(U, Nb) <sub>1</sub> (Va) <sub>3</sub>	U	$\phi_U^{U:Va}: -112127.11 - 132.24 \times T$ [8]
		$\phi_U^{Nb:Va}: -387210.79 - 127.09 \times T$ [8]
		${}^0 \phi_U^{Nb,U:Va}: 81130.73$
	Nb	${}^1 \phi_U^{Nb,U:Va}: 491786.57 - 357.62 \times T$
		$\phi_{Nb}^{Nb:Va}: -395598.95 - 82.03 \times T$ [8]
		$\phi_{Nb}^{U:Va}: -107072.73 - 181.63 \times T$ [8]
		${}^0 \phi_{Nb}^{Nb,U:Va}: -256479.19 + 135.86 \times T$
		${}^1 \phi_{Nb}^{Nb,U:Va}: -205726.88$

**Table 3**

$\gamma_2/\alpha + \gamma_2$  phase boundary data. Here, bulk alloy  $\gamma_1$  is U-17.4 at.% Nb. X-ray measurements of  $\gamma_2$  compositions after long-period aging were carried out at 500 °C, 550 °C and 600 °C. Experimental results indicate that  $\gamma_2$  composition tends to increase with increasing annealing period.

T (°C)	Annealing time (h)	$\gamma_2$ composition (at.% Nb)
500	5300	73.5
500	17532	73.9
500	43830	79.0
550	5300	73.4
550	17532	76.5
600	5300	73.6
600	10600	73.9
625	10600	71.0

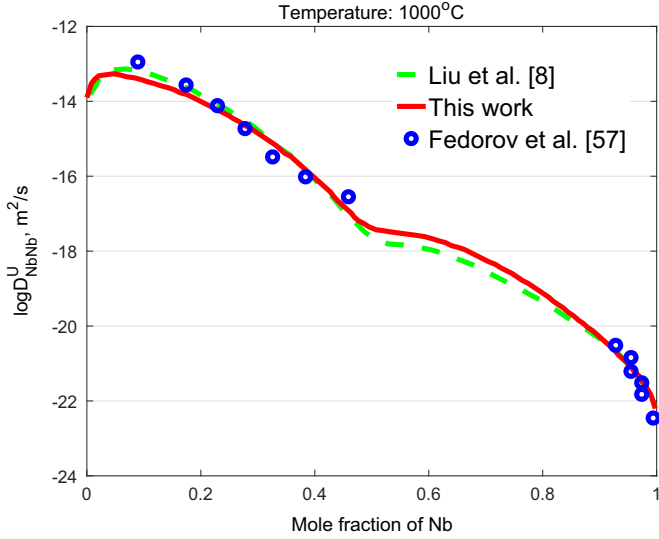


Fig. 8. Calculated interdiffusivity of U–Nb system at 1000 °C as compared to previous calculation [8] and experiment [57].

#### 4.2. Results and discussions

Optimization results are shown in Table 4. Fig. 8 compares the present calculated interdiffusion coefficients at 1273 K with ones from experiment [57] and previous calculations [8]. It can be seen from the figure that the present calculated interdiffusivity at 1000 °C is compatible with the previous calculation [8] as well as experiment [57]. This justifies the current CALPHAD assessment of atomic mobility and diffusivity. Here, it is noted that the diffusion assessment is limited to only bcc U–Nb. This is due to the lack of kinetic data for the other phases, for instance the orthorhombic  $\alpha$ -phase which is of particular interest when discontinuous precipitation is considered [5]. The current results may, however, serve as references for estimating the diffusivities of the missing phases, based on common knowledge such as atomic packing factor.

### 5. Bayesian calibration of model uncertainty

Uncertainty analysis, although well-established and a crucial factor in many areas, is not very common to materials science and engineering. This is notably true to computational thermodynamics, which is of our particular interest and an important branch in materials science and engineering. Pioneering works on the analysis of uncertainty associated with equilibrium phase diagram such as Königsberger [58], Olbricht et al. [59], Chatterjee et al. [60,61], Malakhov [62], Acker et al. [63], and Stan et al. [64] have not attracted much attention. This situation, however, has started to change in recent years, with the introduction of the interesting ICME concept [65]. The role of uncertainty analysis has, within this concept, been revisited in the framework of cross-scale modeling and become more increasingly important. As “CALPHAD software is arguably the most important (and perhaps the only) generic tool available for ICME” [65], it is required that computational thermodynamics must comprehend uncertainty analysis in its account and the early works to be appreciated and carried on. This motivates the following uncertainty analysis of CALPHAD model based on the Bayes' theorem [66].

#### 5.1. Computational details

##### 5.1.1. Bayesian uncertainty analysis

Bayes' theorem was originally proposed by Reverend Thomas Bayes [66] in 1765, based on the law of conditional probabilities. It generally updates the prior knowledge about the model parameters into posterior distributions using the available experimental data, and also provides a formal way to determine how reliable a theory or a hypothesis is, given that some evidence priorly exists. Using this theorem, one can evaluate the reliability/uncertainty of the thermodynamic model by defining the prior probability distribution functions for the model parameters in light of available experimental and first-principles phase-equilibria and thermochemistry data. In particular, the Bayes' theorem reads:

$$P(\theta|D) = \frac{P(D|\theta)P(\theta)}{P(D)} = \frac{P(D|\theta)P(\theta)}{\int P(D|\theta)P(\theta)d\theta} \quad (9)$$

where, in this work, the probability distribution  $P(\theta)$  reflects the prior knowledge about the model parameter  $\theta$ : a vector containing  $a_v^\phi$  and  $b_v^\phi$  parameters in Eq. (4),  $P(D|\theta)$  is the likelihood of the model parameter  $\theta$  given experimental or first-principles data  $D$ , and  $P(D) = \int P(D|\theta)P(\theta)d\theta$  is the probability distribution of experimental data  $D$  without regarding the parameter  $\theta$ , it is also known as the marginal distribution or normalizing constant. These probabilities together define the posterior distribution  $P(\theta|D)$  that describes how well the model parameter  $\theta$  can satisfy the agreement between model output  $M$  and experimental data  $D$ . From this distribution, the variance–covariance matrix defining the uncertainty of the thermodynamic model is computed as:

$$C^\theta = \int (\theta - \langle \theta \rangle)(\theta - \langle \theta \rangle)^T P(\theta|D)d\theta \quad (10)$$

where,  $\langle \theta \rangle$  is the center of gravity of  $P(\theta|D)$ . It is evaluated as:

$$\langle \theta \rangle = \int \theta P(\theta|D)d\theta \quad (11)$$

The implementation of Bayes' theorem and derivations of its statistical properties are generally problematic when  $\theta$  is high-dimensional. In such a case, the integrals required by the theorem (Eq. (9)) and subsequent statistic models (Eqs. (10) and (11)) are difficult to solve, i.e. closed-form expressions are not available and conventional approaches to numerical integrations (e.g. Riemann sum) yield large error. One feasible approach to cope with this would be the use of the Monte Carlo integration. Monte Carlo integration is a numerical technique for estimating high-dimensional integrals on the statistical basis of random sampling. Within this approach, the variance–covariance matrix can simply be evaluated as follows:

$$C^\theta \approx \frac{1}{N} \sum_{i=0}^N \left( \theta_i - \langle \theta \rangle \right) \left( \theta_i - \langle \theta \rangle \right)^T \quad (12)$$

where,

$$\langle \theta \rangle \approx \frac{1}{N} \sum_{i=0}^N \theta_i \quad (13)$$

and,  $\theta_{i=1,2,\dots,N}$  can be sampled from  $P(D|\theta)$ , using different methods such as the direct sampling, the rejection sampling, and the Markov Chain Monte Carlo (MCMC) sampling.

The usage of Monte Carlo integration for Bayesian parameter calibrations and uncertainty analysis of thermodynamic models has previously been introduced by Olbricht et al. [59], Chatterjee et al. [60,61], and Stan et al. [64]. In the former works of Olbricht et al. and Chatterjee et al., the Markov Chain Monte Carlo (MCMC)

method based on Gibbs sampler has been proposed while in the latter work of Stan et al., generic algorithm (GA) sampler was suggested. In the current work, we propose the use of Metropolis–Hastings [68,69] MCMC sampler as another mean to assess the uncertainty of CALPHAD thermodynamic model. Comparisons between Metropolis–Hastings with other approaches is out of the scope of this work but could be found elsewhere (Metropolis–Hastings vs Gibbs) or an interesting topic for a more methodology-oriented study (Metropolis–Hastings vs GA). Details of the Metropolis–Hastings algorithm are mentioned as follows.

### 5.1.2. Markov chain Monte Carlo: Metropolis–Hastings algorithm

Within the Metropolis–Hastings approach, the sampling process is governed by the Metropolis–Hastings ratio, which reads:

$$r_{M-H} = \frac{\frac{P(D|\theta_{cand})P(\theta_{cand})q(\theta_i|\theta_{cand})}{P(D)}}{\frac{P(D|\theta_i)P(\theta_i)q(\theta_{cand}|\theta_i)}{P(D)}} = \frac{P(D|\theta_{cand})P(\theta_{cand})q(\theta_i|\theta_{cand})}{P(D|\theta_i)P(\theta_i)q(\theta_{cand}|\theta_i)} = \frac{\pi(\theta_{cand})q(\theta_i|\theta_{cand})}{\pi(\theta_i)q(\theta_{cand}|\theta_i)} \quad (14)$$

where,  $\theta_{cand}$  is the currently evaluated parameter candidate,  $\theta_i$  is the last accepted parameter of the sampling process,  $\frac{\pi(\theta_{cand})}{\pi(\theta_i)}$  is the Metropolis ratio between the joint distributions of new random sample and the last accepted parameter,  $\frac{q(\theta_i|\theta_{cand})}{q(\theta_{cand}|\theta_i)}$  is the Hastings ratio of proposal density,  $q$ , for interchange probability between  $\theta_i$  and  $\theta_{cand}$ . It should be noted that the use of  $P(D|\theta)P(\theta)$  in place of  $P(D|\theta)$  (for sampling  $\theta_i$  that are required for estimating Eqs. (12) and (13)) is possible since  $P(D)$  is a constant and can be canceled out in the Metropolis–Hastings ratio. This means that there is no need to go through the difficulty of solving the corresponding integral  $P(D) = \int P(\theta)P(D|\theta)d\theta$ .

Based on the Metropolis–Hastings ratio, the Monte Carlo sampling process happens according to the following steps. First, a parameter  $\theta_0$  is chosen as an initial value for the Markov Chain process. It follows by the random sampling of  $\theta_1$  from the proposal distribution  $q$ . The Metropolis–Hastings ratio between  $\theta_0$  and  $\theta_1$  will then be evaluated; and, the minimum between this ratio and 1 will in turn be compared with a random value generated between 0 and 1. If the ratio was larger than the random value,  $\theta_1$  would be accepted to the Markov Chain. Otherwise, there will be no update and  $\theta_0$  will be assigned to  $\theta_1$ . In the next step,  $\theta_2$  will be randomly sampled from  $q$  and  $\theta_1$  will serve as the reference for accepting or rejecting  $\theta_2$  according to the Metropolis–Hastings ratio. In this way, the Metropolis–Hastings MCMC continues until a large number of accepted parameters is collected. These values will then allow the estimation of the uncertainty of the model parameters, according to Eqs. (12) and (13).

### 5.1.3. MCMC computational approach

In the current work, we make use of the Matlab MCMC toolbox by Haario et al. [71,72] to carry out the Metropolis–Hastings algorithm for the uncertainty analysis of the thermodynamic model. For the proposal distribution  $q$ , the adaptive normal distribution, proposed in [71] is utilized. In this adaptive scheme, the mean of the proposal distribution is set at the last accepted parameter and the variance of the distribution is estimated from the ensemble of accepted parameters.

For the prior, we assume a uniform distribution with min and max values specified as  $\bar{\theta} - 3 \times \bar{\sigma}$  and  $\bar{\theta} + 3 \times \bar{\sigma}$ , respectively, where  $\bar{\theta}$  is a vector contains the above assessed parameters (Table 1). Here, the choice of uniform distribution is to allow an equal chance for all parameters around  $\bar{\theta}$  to be investigated by means of MCMC. This tends to minimize unnecessary bias that could have

been placed on the assessed parameters.

The likelihood function is chosen to be a normal distribution, whose mean and variance are the experimental data  $D$  and their errors, respectively. Here,  $D$  consists of the available phase-boundary and thermochemistry data, used in the above thermodynamic assessment. Since the errors of these data are not available, variance is considered as a hyper-parameter with an arbitrary initial value ( $\sigma_0^2 = 0.01^2$ ) which can be updated during MCMC sampling according to the Bayesian framework:

$$P(\sigma^2|D) \propto P(\sigma^2)P(D|\sigma^2) \quad (15)$$

where  $P(\sigma^2|D)$  is the posterior distribution for  $\sigma^2$  that is a conditional probability of  $\sigma^2$  given the experimental data  $D$ ,  $P(D|\sigma^2)$  is an exponential likelihood function, and  $P(\sigma^2)$  is the prior distribution for  $\sigma^2$  that can be considered as a non-informative inverse-gamma distribution  $Inv - \chi^2(N_0, \sigma_0^2)$  with  $N_0 = 1$ . Since the inverse-gamma distribution is the conjugate prior density for the exponential likelihood, the posterior would be also proportional to an inverse-gamma distribution  $Inv - \chi^2(\frac{N_0 + N}{2}, \frac{N_0\sigma_0^2 + N\nu}{2})$  where  $N$  is the number of sampled  $\sigma^2$  and  $\nu = \frac{1}{N} \sum_{i=1}^N (M - D)^2$  with model output  $M(\theta)$ . The details corresponding to the posterior calculation have been mentioned in the book of Gelman et al. [73]. During MCMC parameter generations, the variance is sampled from the inverse-gamma posterior distribution obtained at  $\theta_{cand}$  (for numerator of Eq. (14)) or  $\theta_i$  (for denominator of Eq. (14)). It is worth noting that the variance  $\sigma^2$ , like the model parameters  $\theta$ , should be converging to a mean value, when the number of samples within the MCMC ensemble is large enough.

It should also be noted that the current choice of likelihood and prior functions is quite typical and simple enough that it actually allows an explicit expression of the posterior. This, however, does not solve the high dimensionality problem of the integrals for the estimation of the variance–covariance matrix (Eq. (10)), and therefore, the need for the Monte Carlo integration remains.

### 5.1.4. Propagation of uncertainty

Uncertainty analysis is not only about quantifying the variances of model parameters but also about estimating how much such variances can affect the outputs of the model. This is known as the propagation of uncertainty. In the current work, the propagation of parameter uncertainty to thermodynamic outputs, e.g. phase equilibria and thermochemistry data, is estimated according to:

$$C^M = J C^\theta J^T \quad (16)$$

where,  $C^M$  is the variance–covariance matrix of model function,  $C^\theta$  is the variance–covariance matrix of parameter  $\theta$  evaluated by Eq. (12), and  $J$  is the Jacobian matrix of the partial derivatives of model function with respect to  $\theta$ , evaluated at  $\langle \theta \rangle$ .

## 5.2. Results and discussion

MCMC was carried out to sample for 20,000 parameter candidates. The results are shown in Fig. 9 for twelve  $a_i^\phi$  and  $b_i^\phi$  parameters (see Eq. (4)) used to define the liquid, orthorhombic, tetragonal, and bcc phases. As can be seen from this figure, after just a first few hundred iterations, the parameters has already started to oscillate around their mean values. This indicates that MCMC has converged to its steady state and the reason for this rapid convergence is because the initial  $\theta_0$  chosen for starting the MCMC simulation constitutes of the above assessed parameters (see Table 1) which are already close to the mean values..

Fig. 10 shows the correlation between some selective parameters of the liquid and bcc phases. As can be seen from this figure, the density of sample points increases as these parameters



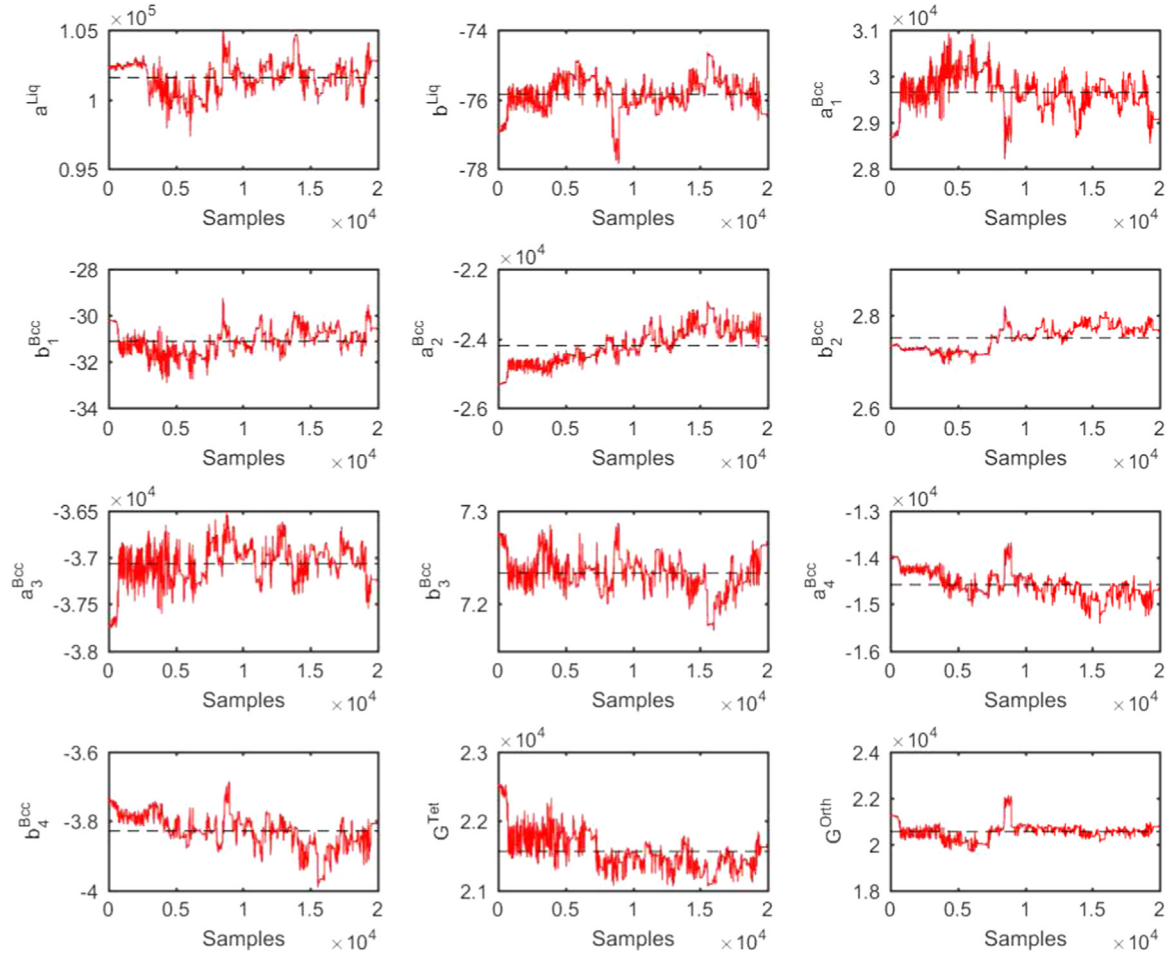


Fig. 9. Candidate parameters selected by the Metropolis-Hastings over 20,000 iterations (dash lines indicate mean values).

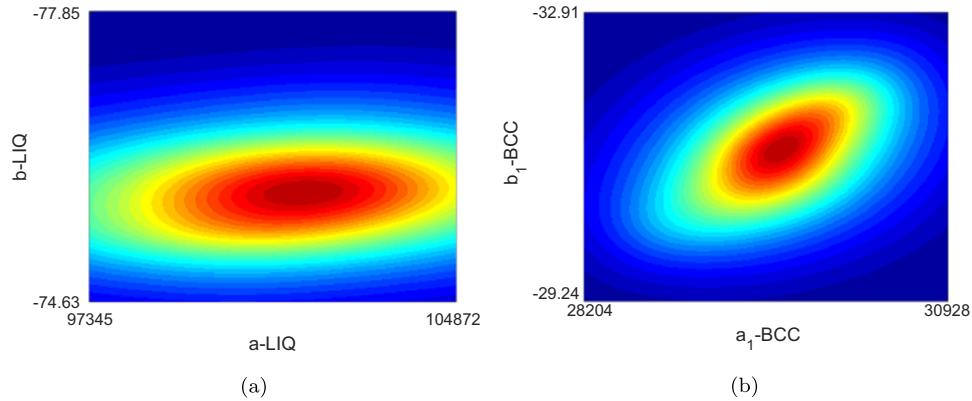


Fig. 10. Correlation between (a) liquid  $a$  and  $b$  parameters and (b) bcc  $a_1$  and  $b_1$  parameters.

get closer to the center of the ellipsoidal distribution, where the probability of having the parameters is the highest. This also indicates that the parameters have converged to their plausible mean values over MCMC sampling. Note that these values are the mean values of the resulting samples, and are relatively close to the values assessed by the Thermo-Calc package, as can be seen in Table 6.

Upon convergence of the model parameters, the variance–covariance matrix is estimated and the results are shown in Table 5. The means and standard deviations summarizing the uncertainties of model parameters are reported in Table 6. The uncertainties of model parameters are in turn propagated to the

model thermochemistry and phase-boundary outputs with 95%-Bayesian confidence interval ( $\pm 2\sigma$ ), and the results are shown in Fig. 10 (a) & (b). Noted that in order to achieve Fig. 10 (b), we relied on a Matlab constrained nonlinear solver, which was used to estimate the model function whose output  $M$  are phase boundaries. These model outputs were required to estimate the likelihood function in MCMC sampling (Eq. (14)) as well as the Jacobian matrix in the propagation of uncertainty (Eq. (16)). The solver overall worked very well but was not very efficient with the  $\alpha + \beta$  region where the tie-line distances, separating the two phases, are too small. Consequently, we were not able to assess the uncertainty of phase equilibria associated with this region.

**Table 5**

Variance–covariance matrix of model parameters ( $\Sigma^A$ ) achieved from 20, 000 MCMC samples. Here, the variances and covariance correspond to the 12 parameters shown in Table 6 in the order from left to right and top to bottom.

	$\sigma_1$	$\sigma_2$	$\sigma_3$	$\sigma_4$	$\sigma_5$	$\sigma_6$	$\sigma_7$	$\sigma_8$	$\sigma_9$	$\sigma_{10}$	$\sigma_{11}$	$\sigma_{12}$
$\sigma_1$	1.26e + 06	−3.41e + 02	−3.78e + 05	4.01e + 02	8.89e + 03	1.18e + 01	−1.02e + 04	2.83e + 00	1.41e + 05	1.65e + 01	4.07e + 03	2.57e + 05
$\sigma_2$	−3.40e + 02	2.29e − 01	1.39e + 02	−8.51e − 02	1.03e + 02	−4.03e − 04	1.08e + 01	−7.26e − 03	−1.02e + 02	−1.83e − 02	−4.34e + 1	−1.47e + 02
$\sigma_3$	−3.78e + 05	1.39e + 02	1.78e + 05	−2.12e + 02	−1.74e + 04	−6.16e + 00	3.55e + 04	−2.07e + 00	−3.92e + 04	−3.51e + 00	−2.58e + 04	−1.20e + 05
$\sigma_4$	4.01e + 02	−8.51e − 02	−2.12e + 02	3.13e − 01	1.17e + 02	1.14e − 02	−4.55e + 01	−1.53e − 03	−6.02e + 00	−7.38e − 03	2.09e + 00	1.18e + 02
$\sigma_5$	8.89e + 03	1.03e + 02	−1.74e + 04	1.17e + 02	2.52e + 05	1.09e + 01	3.32e + 04	−5.85e + 00	−1.16e + 05	−2.05e + 01	−1.07e + 05	−1.71e + 04
$\sigma_6$	1.18e + 01	−4.03e − 04	−6.16e + 00	1.14e − 02	1.09e + 01	6.78e − 04	9.52e − 01	−2.04e − 04	−3.03e + 00	−7.34e − 04	−4.27e + 00	4.0e + 00
$\sigma_7$	−1.02e + 04	1.08e + 01	3.55e + 04	−4.55e + 01	3.32e + 04	9.52e − 01	4.31e + 04	−9.56e − 01	−6.02e + 03	−6.99e − 01	−4.84e + 04	2.76e + 02
$\sigma_8$	2.83e + 00	−7.26e − 03	−2.07e + 00	−1.53e − 03	−5.85e + 00	−2.04e − 04	−9.56e − 01	3.90e − 04	2.99e + 00	7.97e − 04	2.82e + 00	2.96e + 00
$\sigma_9$	1.41e + 05	−1.02e + 02	−3.92e + 04	−6.02e + 00	−1.16e + 05	−3.03e + 00	−6.02e + 03	2.99e + 00	8.10e + 04	1.21e + 01	4.09e + 04	5.87e + 04
$\sigma_{10}$	1.65e + 01	−1.83e − 02	−3.51e + 00	−7.38e − 03	−2.05e + 01	−7.34e − 04	−6.99e − 01	7.97e − 04	1.21e + 01	2.37e − 03	7.18e + 00	7.50e + 00
$\sigma_{11}$	4.07e + 03	−4.34e + 01	−2.58e + 04	2.09e + 00	−1.07e + 05	−4.27e + 00	−4.84e + 04	2.82e + 00	4.09e + 04	7.18e + 00	7.66e + 04	5.09e + 03
$\sigma_{12}$	2.57e + 05	−1.47e + 02	−1.20e + 05	1.18e + 02	−1.71e + 04	4.0e + 00	2.76e + 02	2.95e + 00	5.87e + 04	7.50e + 00	5.09e + 03	1.25e + 05

**Table 6**

Mean values of the model parameters achieved from 20, 000 MCMC samples. Here, the marginalized parameter uncertainties are obtained by taking the square root of the variances shown in Table 5.

Phase	Model	Parameters
Liquid	(Nb, U) <sub>1</sub>	$G_{Nb,U}^{liq} : 101574.37 \pm 1123 - 75.85 \pm 0.48 T$
Bcc	(Nb, U) <sub>1</sub> (V) <sub>a3</sub>	$G_{Nb,U}^{bcc} : 29651.38 \pm 421.77 - 31.11 \pm 0.56 T$ $G_{Nb,U}^{bcc} : -24196.27 \pm 502.08 + 2.75 \pm 0.03 T$ $G_{Nb,U}^{bcc} : -37069.50 \pm 207.67 + 7.23 \pm 0.02 T$ $G_{Nb,U}^{bcc} : -14588.82 \pm 284.65 - 3.83 \pm 0.05 T$
Tet.	(Nb, U) <sub>1</sub>	$G_{Nb,U}^{tet} = G_{Nb,U}^{bcc} + 21560.86 \pm 276.72$
Orth.	(Nb, U) <sub>1</sub>	$G_{Nb,U}^{orth} = G_{Nb,U}^{bcc} + 20542.57 \pm 354.06$

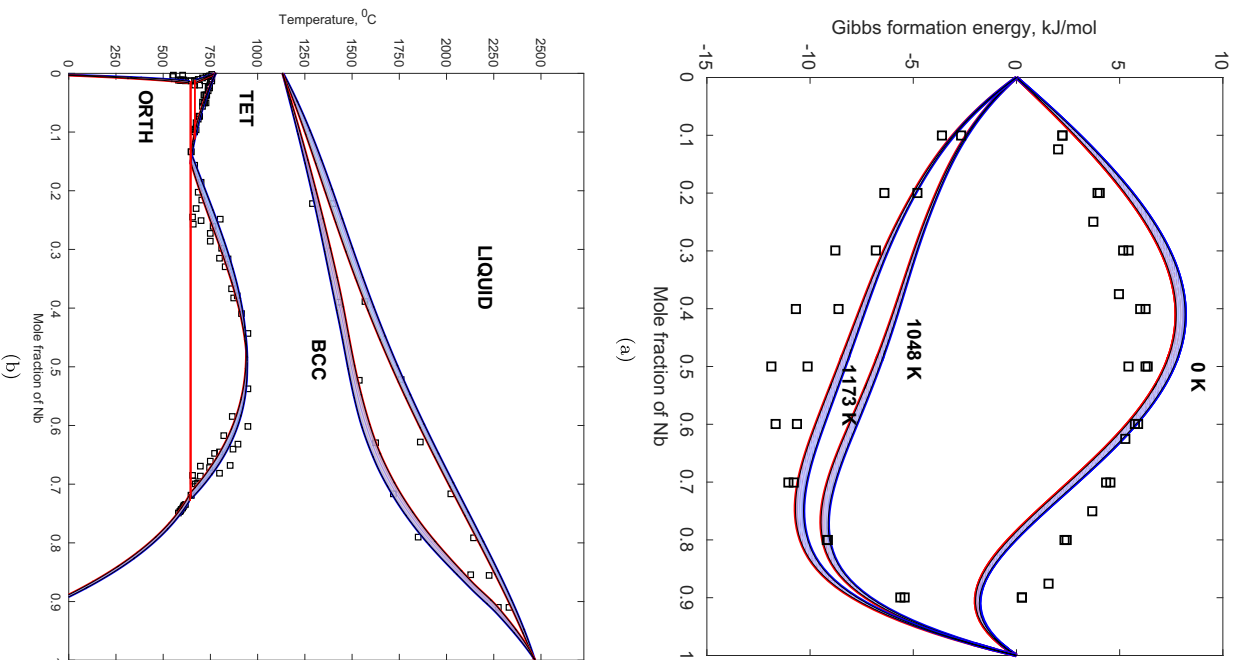


**Fig. 11.** Bayesian phase diagram and selective  $\gamma$ -formation energies (small squares indicate experimental/evaluated phase boundaries and ab initio energies).

As shown in Fig. 11 (b), the band is the largest for the liquid phase compared to other phases. Although a small uncertainty should be expected within this region, due to the fact that only one single dataset (i.e. [9]) is given to the MCMC simulation, the result still predicts the highest uncertainty band in relative to the other phases. This is interestingly consistent with the fact that the liquidus and solidus were reported to be very difficult to observe [9].

The uncertainty bands of bcc, tetragonal, and orthorhombic phases as well as the Gibbs formation energies are fairly small. It should be noted here that these small bands are the result of imposing a high weighting factor on the monotectoid invariance, whose values are taken from the result of this work (see Table 2), during the MCMC evaluation of uncertainty of model parameters. As experienced by the authors, a smaller weighting factor for this invariance resulted in a larger uncertainty for all phases, with liquid still being the phase with the largest uncertainty.

From here, an interesting take-away idea would be that with the help of Bayesian CALPHAD the effort in evaluating a reliable phase diagram could be significantly minimized by only focusing on the measurements of some important data (e.g. monotectoid invariance) with a high level of confidence (to justify the use of large weighting factor) and let the Bayesian CALPHAD elaborate the results from these data together with other (less accurate) available experiments.

Lastly, despite not being reported in this work, a similar analysis can be readily accomplished to investigate the propagation of the thermodynamic model's uncertainty to the kinetic diffusivities using Eq. (16) with some predefined kinetic-model parameters, as shown in Table 4. One step beyond this is to the Bayesian assessment of the kinetic parameters; although it is not so much straightforward.

## 6. Conclusion

To conclude, the thermodynamics and kinetic diffusivity of U–Nb are revisited by means of theoretical and experimental approaches. In particular, first-principles calculations are coupled with the CALPHAD method to assess the thermodynamic properties of U–Nb. Assessment result is generally consistent with experiments, evaluations, and previous calculations. In exception, the calculated  $\alpha + \gamma_2$  two phase region is considerably larger than that suggested by previous work. This difference is believed to result from the usage of ab initio energetic data which tends to suggest a small uranium-solubility within Nb-rich alloys. To resolve this problem, long-aged experiments are carried out at the longest time of 5 years to measure reliable phase equilibria data at the  $\gamma_2/\alpha + \gamma_2$  boundary. It has been shown that the experiment remarkably agrees with the current calculation. This firstly verifies the reliability of the current thermodynamic assessment. Secondly, it demonstrates the advantage and, to a certain extent, predictability of the mutual-consistent coupling between first-principles calculations and the CALPHAD approach. The thermodynamic descriptions is then used to evaluate the atomic mobility and diffusivity of  $\gamma$ -U–Nb, also with the CALPHAD framework. The assessment result, in this case, also shows reasonable agreement with experiments and previous calculation. Lastly, to encourage a routine practice of model-uncertainty analysis in computational thermodynamics and kinetics, Bayesian Metropolis–Hastings (MCMC) approach is carried out to assess the uncertainty of the CALPHAD thermodynamic model and its propagation to the calculated thermochemistry data and phase diagram. It is hoped that the thermodynamic and kinetic-diffusivity descriptions achieved in this work would contribute to the establishment of an essential and sound background for future studies of microstructure

evolutions in U–Nb, which are essential for evaluating the fuel's performance, and also for assessing the thermodynamic and kinetic properties of advanced multi-component metallic fuels, which are developed upon the promising binary fuel.

## Acknowledgements

This work was performed under the auspices of the United States Department of Energy by the Lawrence Livermore National Laboratory and Los Alamos National Laboratory under contract Nos. DE-AC52-07NA27344 and DE-AC52-06NA25396, respectively. TCD acknowledges the partial support of NSF through grant DMR-1410983. RA also acknowledges partial support of NSF through grant CMMI-1534534. TCD specially thanks Prof. I. Steinbach, Dr. O. Shchyglo, Dr. R.D. Kamachali, M. Stratmann, A.A. Gießmann, and E. Borukhovic for helpful discussions regarding phase-field theory and the interface dissipation model. R.E.H., H.M.V., A.L., A.I. S., and G.K. acknowledges experimental assistance from T.J. Tucker and P.A. Papin. First-principles calculations were carried out in the Chemical Engineering Cluster and the Texas A&M Supercomputing Facility at Texas A&M University as well as in the Ranger Cluster at the Texas Advanced Computing Center at University of Texas, Austin.

## References

- [1] R. Vandermeer, Phase transformations in a uranium-14 at% niobium alloy, *Acta Metall.* 28 (1980) 383–393.
- [2] K. Eckelmeyer, A. Romig, L. Weirick, The effect of quench rate on the microstructure, mechanical properties, and corrosion behavior of U-6 wt pct Nb, *Metall. Trans. A* 15 (7) (1984) 1319–1330.
- [3] H.M. Volz, R.E. Hackenberg, A.M. Kelly, W. Hults, A. Lawson, R. Field, D. Teter, D. Thoma, X-ray diffraction analyses of aged U–Nb alloys, *J. Alloy. Compd.* 444–445 (2007) 217–225.
- [4] A. Clarke, R. Field, R. Hackenberg, D. Thoma, D. Brown, D. Teter, M. Miller, K. Russell, D. Edmonds, G. Beverini, Low temperature age-hardening in U-13 at% Nb: an assessment of chemical redistribution mechanisms, *J. Nucl. Mater.* 393 (2009) 282–291.
- [5] R.E. Hackenberg, H.M. Volz, P.A. Papin, A.M. Kelly, R.T. Forsyth, T.J. Tucker, K. D. Clarke, Kinetics of lamellar decomposition reactions in U–Nb alloys, *Solid State Phenom.* 172 (2011) 555–560.
- [6] I. Manna, S. Pabi, W. Gust, Discontinuous reactions in solids, *Int. Mater. Rev.* 46 (2001) 53–91.
- [7] X. Liu, Z. Li, J. Wang, C. Wang, Thermodynamic modeling of the U–Mn and U–Nb systems, *J. Nucl. Mater.* 380 (1) (2008) 99–104.
- [8] Y. Liu, D. Yu, Y. Du, G. Sheng, Z. Long, J. Wang, L. Zhang, Atomic mobilities, diffusivities and their kinetic implications for U–X (X = Ti, Nb and Mo) bcc alloys, *CALPHAD* 37 (2012) 49–56.
- [9] B. Rogers, D. Atkins, E. Manthos, M. Kirkpatrick, Uranium–columbium alloy diagram, *Trans. Met. Soc. AIME* 212 (1958) 387–393.
- [10] P. Pfeil, J. Browne, G. Williamson, The uranium–niobium alloy system in the solid state, *J. Inst. Met.* 87 (1958–59) 204–208.
- [11] J. Koike, M. Kassner, R. Tate, R. Rosen, The Nb–U (niobium–uranium) system, *J. Phase Equilibria* 19 (3) (1998) 253–260.
- [12] T.B. Massalski, H. Okamoto, P. Subramanian, L. Kacprzak, et al., *Binary Alloy Phase Diagrams*, ASM International, Russell Township, Geauga County, Ohio, 1990.
- [13] S. Bajaj, A. Landa, P. Söderlind, P.E. Turchi, R. Arróyave, The U–Ti system: strengths and weaknesses of the CALPHAD method, *J. Nucl. Mater.* 419 (1) (2011) 177–185.
- [14] B. Sundman, H. Seifert, F. Aldinger, The Ringberg Workshop 1996 on solution modelling, *CALPHAD* 21 (2) (1997) 139–141.
- [15] B. Sundman, F. Aldinger, H. Seifert, The Ringberg workshop 1997 on the application of computational thermodynamics, *CALPHAD* 24 (1) (2000) 15–17.
- [16] B.P. Burton, N. Dupin, S.G. Fries, G. Grimvall, A.F. Guillermet, O. Miodownik, W. Alan, V. Vinograd, Using ab initio calculations in the CALPHAD environment, *Z. Met.* 92 (6) (2001) 514–525.
- [17] J.-O. Andersson, J. Agren, Models for numerical treatment of multicomponent diffusion in simple phases, *J. Appl. Phys.* 72 (4) (1992) 1350–1355.
- [18] H.J. Monkhorst, J.D. Pack, Special points for brillouin-zone integrations, *Phys. Rev. B* 13 (12) (1976) 5188.
- [19] B. Gyorffy, Coherent-potential approximation for a nonoverlapping-muffin-tin-potential model of random substitutional alloys, *Phys. Rev. B* 5 (6) (1972) 2382.
- [20] I. Abrikosov, A. Niklasson, S. Simak, B. Johansson, A. Ruban, H.L. Skriver, Order-

- NGreen's function technique for local environment effects in alloys, *Phys. Rev. Lett.* 76 (22) (1996) 4203.
- [21] O.E. Peil, A.V. Ruban, B. Johansson, Self-consistent supercell approach to alloys with local environment effects, *Phys. Rev. B* 85 (16) (2012) 165140.
  - [22] P.E. Blöchl, Projector augmented-wave method, *Phys. Rev. B* 50 (24) (1994) 17953.
  - [23] G. Kresse, D. Joubert, From ultrasoft pseudopotentials to the projector augmented-wave method, *Phys. Rev. B* 59 (3) (1999) 1758.
  - [24] G. Kresse, J. Hafner, Ab initio molecular dynamics for liquid metals, *Phys. Rev. B* 47 (1) (1993) 558.
  - [25] G. Kresse, J. Hafner, Ab initio molecular-dynamics simulation of the liquid-metal-amorphous-semiconductor transition in germanium, *Phys. Rev. B* 49 (20) (1994) 14251.
  - [26] G. Kresse, J. Furthmüller, Efficient iterative schemes for ab initio total-energy calculations using a plane-wave basis set, *Phys. Rev. B* 54 (16) (1996) 11169.
  - [27] A. Zunger, S.-H. Wei, L. Ferreira, J.E. Bernard, Special quasirandom structures, *Phys. Rev. Lett.* 65 (3) (1990) 353.
  - [28] A. Van de Walle, P. Tiwary, M. De Jong, D. Olmsted, M. Asta, A. Dick, D. Shin, Y. Wang, L.-Q. Chen, Z.-K. Liu, Efficient stochastic generation of special quasirandom structures, *Calphad* 42 (2013) 13–18.
  - [29] F. Cervera, et al., ASM Ready Reference: Thermal Properties of Metals, ASM International, Russell Township, Geauga County, Ohio, 2002.
  - [30] P. Söderlind, B. Sadigh, V. Lordi, A. Landa, P. Turchi, Electron correlation and relativity of the 5-f electrons in the U-Zr alloy system, *J. Nucl. Mater.* 444 (1) (2014) 356–358.
  - [31] R. Jackson, Reversible martensitic transformation between transition phases of Uranium-base Niobium alloys, Dow Chemical Co., Golden, Colorado, Rocky Flats Div., Report RFP-1535, 1 January 1970.
  - [32] B. Sawyer, The uranium–columbium alloy system, Argonne Lab Report ANL-4027, October 1946.
  - [33] H. Saller, F. Rough, Alloys of uranium with zirconium, chromium, columbium, vanadium, and molybdenum, Battelle, USA, Report BMI-752, United States Atomic Energy Commission, 1952.
  - [34] O. Ivanov, G. Terekhov, Transformations of the  $\gamma$ -solid solution during quenching and tempering in the uranium–niobium and uranium–niobium–molybdenum systems, *Struct. Alloy. Certain Syst. Contain. Uranium Thorium* (1961) 249–264.
  - [35] M. Hansen, K. Anderko, H.W. Salzberg, Constitution of binary alloys, *J. Electrochem. Soc.* 105 (1958) 260C–261C.
  - [36] G. Terekhov, Features of the structure of the U–Nb phase diagram, *Russ. Metall.* 4 (1982) 170–171.
  - [37] R.P. Elliott, Constitution of Binary Alloys, First-supplement, 2, McGraw-Hill, New York City, New York, 1965.
  - [38] P. Chiotti, V. Akhachinskij, I. Ansara, The chemical thermodynamics of actinide elements and compounds, part 5: the actinide binary alloys, V. Medvedev, M. H. Rand, E.F. Westrum Jr., F.L. Oetting (Eds.) International Atomic Energy Agency, Vienna, 1981.
  - [39] H. Saller, F. Rough, Compilation of U.S. and U.K. uranium and thorium constitutional diagrams, No. BMI-1000. Battelle Memorial Institute, Columbus, OH, USA, 1955.
  - [40] Y. Virgil'ev, Nonmetallic inclusions in alloys of uranium and zirconium, niobium, and molybdenum, the structure of alloys of certain systems containing uranium and thorium; Gosudarstvennoe Izdatel'stvo Literatury v Oblasti Atomnoi Nauki Tekhniki, Moscow 306–311 (1961) in Russian; TR: AEC-tr-5834, U.S. Atomic Energy Comm. (1961) 289–293.
  - [41] C. Peterson, W. Steele, A study of the effect of alloying on the gamma-phase stability of uranium using vacuum differential thermal analysis, No. UCRL-7595. California. Univ., Livermore. Lawrence Radiation Lab., 1963.
  - [42] C. D'Amato, F. Saraceno, T. Wilson, Phase transformations and equilibrium structures in uranium-rich niobium alloys, *J. Nucl. Mater.* 12 (3) (1964) 291–304.
  - [43] C. Fizzotti, A. Maspereni, Effects of heat treatment on the structure of uranium-rich U–Nb alloys, *Com. Naz. Energ. Nucl., RT/MET-(66)* 1 (1966) 1–23.
  - [44] F. Coppola, C. Fizzotti, Metastable phases in uranium-rich U–Nb alloys and their thermal decomposition, *Com. Naz. Energ. Nucl., RT/MET-(66)* 2 (1966) 1–37.
  - [45] L. Gomofov, E. Lyutina, O. Ivanov, Solubility of zirconium, molybdenum, and niobium in alpha-uranium, *Russ. Metall.* 2 (1970) 131–135.
  - [46] B. Djurić, Decomposition of gamma phase in a uranium-9.5 wt% niobium alloy, *J. Nucl. Mater.* 44 (2) (1972) 207–214.
  - [47] Y.V. Vambersky, A. Udovsky, O. Ivanov, Investigation of thermodynamic properties of bcc solid solutions of uranium (ii), the uranium–niobium system, *J. Nucl. Mater.* 55 (1) (1975) 96–108.
  - [48] H. Hardy, A sub-regular solution model and its application to some binary alloy systems, *Acta Metall.* 1 (2) (1953) 202–209.
  - [49] A. Dinsdale, SGTE data for pure elements, *CALPHAD* 15 (4) (1991) 317–425.
  - [50] R. Jackson, Isothermal transformations of uranium-13 atomic percent niobium, Rocky Flats Plant (Golden, CO), report RFP-1609, 9 April 1971.
  - [51] L.-Q. Chen, Phase-field models for microstructure evolution, *Annu. Rev. Mater. Res.* 32 (1) (2002) 113–140.
  - [52] I. Steinbach, Phase-field models in materials science, *Model. Simul. Mater. Sci. Eng.* 17 (7) (2009) 073001.
  - [53] A. Borgenstam, L. Höglund, J. Ågren, A. Engström, DICTRA, a tool for simulation of diffusional transformations in alloys, *J. Phase Equilibria* 21 (3) (2000) 269–280.
  - [54] J.-O. Andersson, T. Helander, L. Höglund, P. Shi, B. Sundman, Thermo-Calc & DICTRA, computational tools for materials science, *CALPHAD* 26 (2) (2002) 273–312.
  - [55] Y. Adda, A. Kirianenko, *J. Nucl. Mater.* 1 (1959) 120.
  - [56] G. Fedorov, V. Gusev, E. Smirnov, Diffusive and thermodynamic properties of gamma-phase of uranium–niobium system alloys, *At. Energi.* 32. 1 (1972) 11.
  - [57] G.B. Fedorov, E.A. Smirnov, Diffusion in reactor materials, *Natl. Bur. Stand.* (1984).
  - [58] E. Königsberger, Improvement of excess parameters from thermodynamic and phase diagram data by a sequential bayes algorithm, *Calphad* 15 (1) (1991) 69–78.
  - [59] W. Olbricht, N.D. Chatterjee, K. Miller, Bayes estimation: A novel approach to derivation of internally consistent thermodynamic data for minerals, their uncertainties, and correlations. part i: Theory, *Phys. Chem. Miner.* 21 (1–2) (1994) 36–49.
  - [60] N.D. Chatterjee, K. Miller, W. Olbricht, Bayes estimation: A novel approach to derivation of internally consistent thermodynamic data for minerals, their uncertainties, and correlations. part ii: Application, *Phys. Chem. Miner.* 21 (1–2) (1994) 50–62.
  - [61] N.D. Chatterjee, R. Kruëger, G. Haller, W. Olbricht, The bayesian approach to an internally consistent thermodynamic database: theory, database, and generation of phase diagrams, *Contrib. Mineral. Petrol.* 133 (1–2) (1998) 149–168.
  - [62] D.V. Malakhov, Confidence intervals of calculated phase boundaries, *Calphad* 21 (3) (1997) 391–400.
  - [63] J. Acker, K. Bohmhammel, Optimization of thermodynamic data of the Ni–Si system, *Thermochim. Acta* 337 (1) (1999) 187–193.
  - [64] M. Stan, B. Reardon, A bayesian approach to evaluating the uncertainty of thermodynamic data and phase diagrams, *Calphad* 27 (3) (2003) 319–323.
  - [65] N. R. C. on Integrated Computational Materials Engineering, Integrated Computational Materials Engineering: a Transformational Discipline for Improved Competitiveness and National Security, National Academies Press, 2008.
  - [66] M. Bayes, M. Price, An Essay towards solving a Problem in the Doctrine of Chance. By the late Rev. Mr. Bayes, communicated by Mr. Price, in a letter to John Canton, A. M. F. R. S., *Phil. Trans. R. Soc. Lond.* 53 (0) 370–418.
  - [68] N. Metropolis, A.W. Rosenbluth, M.N. Rosenbluth, A.H. Teller, E. Teller, Equation of state calculations by fast computing machines, *J. Chem. Phys.* 21 (6) (1953) 1087–1092.
  - [69] W.K. Hastings, Monte Carlo sampling methods using Markov chains and their applications, *Biometrika* 57 (1) (1970) 97–109.
  - [71] H. Haario, E. Saksman, J. Tamminen, An adaptive metropolis algorithm, *Bernoulli* (2001) 223–242.
  - [72] H. Haario, M. Laine, A. Mira, E. Saksman, Dram: efficient adaptive MCMC, *Stat. Comput.* 16 (4) (2006) 339–354.
  - [73] A. Gelman, J.B. Carlin, H.S. Stern, D.B. Rubin, Bayesian Data Analysis, Chapman & Hall/CRC, Boca Raton, FL, USA, 2014.